ENVIRONMENTAL STUDIES

Single rhenium atoms on nanomagnetite: Probing the recharge process that controls the fate of rhenium in the environment

Rongrong Ding[1,2], Carolina Guida[1,3,4], Carolyn I. Pearce[5], Elke Arenholz[5], Jean-Marc Grenèche[6], Alexandre Gloter[7], Andreas C. Scheinost[8], Kristina O. Kvashnina[8], Kaifeng Wang[1,9], Alejandro Fernandez-Martinez[1], Yang Mu[2]*, Kevin M. Rosso[5]*, Laurent Charlet[1]*

Understanding the redox transitions that control rhenium geochemistry is central to paleoredox and geochronology studies, as well as predicting the fate of chemically similar hazardous oxyanions in the environment such as pertechnetate. However, detailed mechanistic information regarding rhenium redox transitions in anoxic systems is scarce. Here, we performed a comprehensive laboratory study of rhenium redox transitions on variably oxidized magnetite nanoparticle surfaces. Through high-end spectroscopic and microscopic tools, we propose an abiotic transition pathway in which aqueous iron(II) ions in the presence of pure or preoxidized magnetite serve as an electron source to reduce rhenium(VII) to individual rhenium(IV) atoms or small polynuclear species on nanoparticle surfaces. Notably, iron(II) ions recharged preoxidized magnetite nanoparticles exhibit a maghemite core and a magnetite shell, challenging the traditional core-shell magnetite-maghemite model. This study provides a fundamental understanding of redox processes governing rhenium fate and transport in the environment and enables an improved basis for predicting its speciation in geochemical systems.

INTRODUCTION

Rhenium (Re) is widely distributed in nature as a trace element, with concentrations ranging from 7.29 to 8.19 pg/g in open seas (i.e., the Pacific Ocean) (*1*). It is highly enriched in sedimentary rocks, where concentrations range from 3 to 1000 ng/g (*2*), and it can reach up to 3 mg/g in porphyry copper deposits (*3*, *4*). Redox conversions from soluble Re heptavalent species [perrhenate (ReO_4^-)] to insoluble tetravalent species [$ReO_{2(s)}$ or $ReS_{2(s)}$] largely constrains the biogeochemical behavior of Re. This redox reaction that leads to the immobilization of Re is of importance in paleoredox studies, where the isotopic signature of Re reduction is used to indicate O_2 fugacity and for geological dating using the rhenium and osmium isotopic ratio (*5*, *6*). Beyond paleoenvironmental applications, Re is also critical in modern environmental contexts, particularly in nuclear waste repository safety assessments and subsurface remediation efforts, as it serves as an analog for the fission product technetium (Tc) (*7*, *8*).

It has been reported that Re is primarily controlled by magnetite in reduced sediments and arc magmas, environments that often exhibit seawater-like pH values (around 8.1 or slightly basic) (*9*–*11*). Magnetite nanoparticles, abundant under anoxic conditions, are mixed-valence spinel-type materials based on Fe^{2+} and Fe^{3+} in octahedral (Oh) and tetrahedral (Td) coordination, with the arrangement of $[Fe^{3+}{\downarrow}]_{Td}[Fe^{3+}{\uparrow}Fe^{2+}{\uparrow}]_{Oh}$ (*12*–*16*). This structure enables the dynamic exchange of Fe^{2+} ions between solid and solution through a topotactic oxidation/reduction process (*17*–*19*). Specifically, magnetite can release Fe^{2+} into solution, and partially oxidized magnetite can conversely take up Fe^{2+} ions from the solution to restore magnetite stoichiometry through a so-called "recharge" process (*20*, *21*). Thus, Fe^{2+} acts as a crucial electron carrier that facilitates electron transfer into and out of the magnetite structure, substantially influencing the mobility and immobilization of redox-sensitive trace metals such as Re in both natural and engineered systems (*22*–*25*). Notably, magnetite has been shown to reductively precipitate trace metals such as chromium, uranium, and selenium, often forming unique structures such as surface nanowires (*23*, *26*) or amorphous layers (*27*–*29*). However, the behavior of Re upon reduction by magnetite remains unknown. Therefore, understanding the interactions between magnetite and Re under environment-relevant conditions is crucial for predicting its redox reactivity and deserves further exploration.

Questions remain regarding the mechanism of magnetite oxidation and recharge. Oxidation of magnetite bulk single crystals involves the outward diffusion of Fe^{2+} to the mineral surface where it is oxidized, yielding a core-shell structure made of magnetite-maghemite (*14*, *30*–*32*). However, recent studies using surface-sensitive x-ray magnetic circular dichroism (XMCD) on magnetite nanoparticles have shown an outer shell enriched in Fe^{2+} (4 nm), while the core would tend toward maghemite (*33*–*36*). This is opposite to the magnetite-maghemite core-shell structure formed with bulk crystals reported previously. Part of the challenge is that there is limited experimental evidence for distinguishing between magnetite and maghemite crystal structures. The lattice constants of the two minerals differ by only 1%, the spinel lattice being retained in both cases, and the extra charge left by the Fe^{2+} vacancy being neutralized by the oxidation of Fe^{2+} to Fe^{3+} in maghemite (*37*, *38*). Consequently,

[1]Institute of Earth Science (ISTerre), Université Grenoble Alpes, Université Savoie Mont Blanc, CNRS, IRD, Université Gustave Eiffel, F-38000 Grenoble, France. [2]CAS Key Laboratory of Urban Pollutant Conversion, Department of Environmental Science and Engineering, University of Science and Technology of China, Hefei, China. [3]STARLAB, Department of Earth and Atmospheric Sciences, Central Michigan University, Brooks Hall 313A, Mount Pleasant, MI 48859, USA. [4]Grupo de Geología Médica y Forense, Universidad Nacional de Colombia, Carrera 30 No. 45-03, Edificio 224, Oficina 411, Bogotá 111321, Colombia. [5]Pacific Northwest National Laboratory, Richland, WA, USA. [6]Institut des Molécules et Matériaux du Mans, IMMM, UMR CNRS 6283, Université du Maine, 72085 Le Mans Cedex, France. [7]Laboratoire de Physique des Solides, Université Paris-Saclay, CNRS UMR 8502, 91405 Orsay, France. [8]European Synchrotron Radiation Facility, 71 avenue des Martyrs, CS 40220, 38043 Grenoble Cedex 9, France. [9]Department of Geochemistry, Geological Survey of Denmark and Greenland (GEUS), Øster Voldgade 10, Copenhagen, Denmark.
*Corresponding author. Email: charlet38@gmail.com (L.C.); Kevin.Rosso@pnnl.gov (K.M.R.); yangmu@ustc.edu.cn (Y.M.)

cutting-edge techniques are needed to explore how the "recharging" process works at the atomic level to determine whether aqueous Fe^{2+} [$Fe^{2+}_{(aq)}$] is swapped with the inner structural Fe atoms in magnetite or with the enriched Fe atoms on the surface. For that purpose, we chose rhenium as a molecular reporter of the surface redox state, using the soluble, weakly binding ReO_4^- oxyanion as the oxidant probe species that, when reduced, deposits as relatively insoluble Re(IV) species. To understand the role of structural versus $Fe^{2+}_{(aq)}$, we examined the interaction of ReO_4^- with nanomagnetites that had been oxidized and recharged to various extents, with and without additional $Fe^{2+}_{(aq)}$.

We examined the reduction kinetics and equilibrium speciation of Re sorbed onto nanomagnetite in the presence of coadsorbed $Fe^{2+}_{(aq)}$ using a multimethod approach. Synchrotron-based x-ray absorption near-edge structure (XANES) spectroscopy, extended x-ray absorption fine structure (EXAFS) spectroscopy, resonant inelastic x-ray scattering (RIXS), and surface-sensitive XMCD, along with bulk-sensitive ^{57}Fe Mössbauer spectrometry and spatially resolved scanning transmission electron microscopy–high-angle annular dark field (STEM-HAADF) with electron energy-loss spectroscopy (EELS), were used to reveal the oxidation and recharging mechanisms of magnetite and the fate of Re. The systematic experimental findings expand our understanding of iron-Re surface redox chemistry. By considering the charge and discharge mechanism of magnetite at the atomic scale, this work provides important theoretical support for further studies of redox recrystallization at mineral-water interfaces.

RESULTS AND DISCUSSION

Effect of Fe(II) resupply and particle recharge

The surface properties and redox reactivity of magnetite in aqueous environments were investigated by equilibrating nanomagnetite with hydrogen peroxide (H_2O_2) at different concentrations to synthesize preoxidized magnetite with a range of x values ($x = Fe^{2+}/Fe^{3+}$ in the solid phase, so $x = 0.5$ for pure magnetite). The wet chemical results (table S1) show that the x values of preoxidized magnetite are similar to those calculated on the basis of the H_2O_2 addition. ^{57}Fe Mössbauer spectrometry shows that the preoxidized magnetite is formed of two phases, magnetite and maghemite, and the fitting of the Mössbauer spectra further demonstrates the successful synthesis of preoxidized magnetite with different oxidation extents close to the expected x values (fig. S1 and table S1).

After establishing our ability to control the extent of preoxidation, preoxidized magnetite nanoparticles ranging in stoichiometry were exposed to Fe^{2+} solutions to "resupply" the surface with reducing equivalents. The amount of Fe^{2+} added was based on the amount needed to bring the preoxidized magnetite (based on H_2O_2 addition) back to $x = 0.5$. The results show that most of the $Fe^{2+}_{(aq)}$ was absorbed by the preoxidized magnetite (fig. S2). After correction with the x values measured by the wet chemical method, the recharging extent was calculated to be even higher than 100% (fig. S2). This is because Fe^{2+} in solution not only acts as an electron donor to recharge the preoxidized magnetite but part of the Fe^{2+} is also adsorbed onto particle surfaces. The results of Mössbauer spectrometry confirm that the preoxidized magnetite has been recharged and reverts to stoichiometric magnetite (fig. S3 and table S1). RIXS spectroscopy further provides information about the distribution of total Fe in the bulk materials (ordered and disordered Fe). Figure 1 (A and B) shows an enlargement of the pre-edge features in the K-edge spectra of preoxidized and recharged magnetite. These spectra have been created by a diagonal cut across the RIXS plane at a constant emission energy (CEE). The spectra have been normalized to highlight the differences in spectral shapes. The pre-edge energy can be characterized by its center of gravity (first moment) and is positioned at 7113 eV for the divalent iron oxides and 7116.5 eV for the trivalent iron oxides (*39*). The preoxidized magnetite exhibits a pronounced shift toward higher edge energy (Fig. 1C), and in the CEE spectrum, the Fe(III) peak is significantly higher compared to pure magnetite (Fig. 1D). Similarly, for recharged magnetite, the absorption peak aligns with the peak in

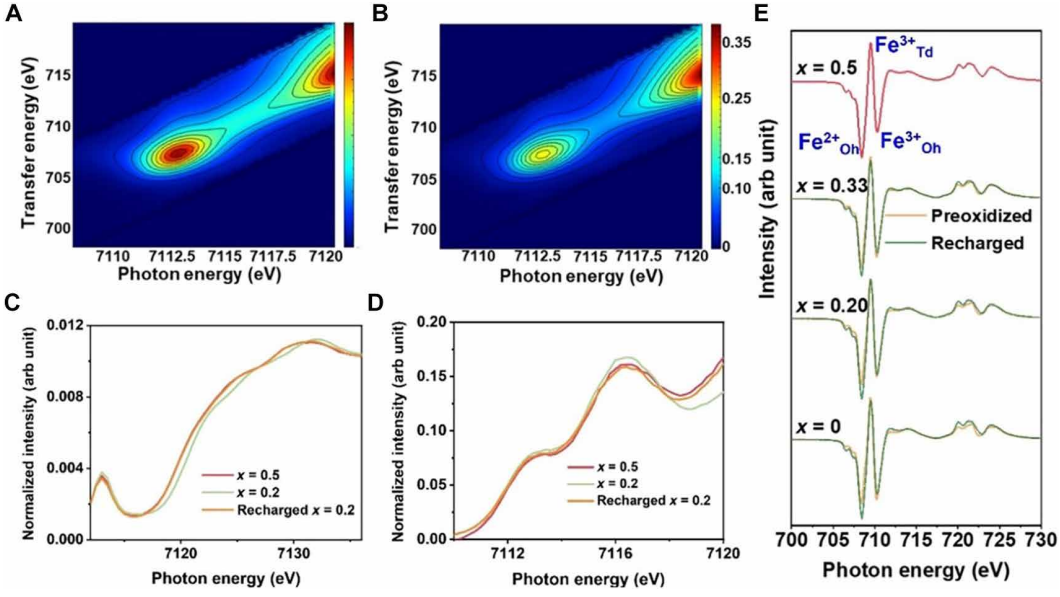

Fig. 1. Spectroscopic characterization of preoxidized and recharged magnetite. 1s2p RIXS planes of (**A**) $x = 0.20$ oxidized magnetite, (**B**) $x = 0.20$ recharged magnetite, and (**C**) related partial fluorescence-yield XANES extracted from RIXS planes using the signal at the maximum of the emission spectra, (**D**) CEE cuts of RIXS spectra, and (**E**) Fe $L_{2,3}$ XMCD of preoxidized and recharged magnetite. Arb unit, arbitrary units.

the spectrum for $x = 0.5$, demonstrating that the magnetite nanoparticles are undergoing oxidation-recharging processes.

XMCD is sensitive to magnetically ordered Fe^{2+} and Fe^{3+}, and all x_{sur} values (Fe^{2+}/Fe^{3+} ratio, with "sur" referring to the near-surface region) of the preoxidized magnetite after reaction with added Fe^{2+} are in agreement with the stoichiometry of the initial magnetite. The recharging process for oxidized magnetite in presence of Fe^{2+} is confirmed (Fig. 1E). Preoxidation results in a decrease in intensity for the peak corresponding to Fe^{2+}_{Oh}, accompanied by an increase in intensity for the peak corresponding to Fe^{3+}_{Oh} (Fig. 1E and table S1), suggesting that the oxidation process is only a redistribution of electrons between Fe in octahedral sites within magnetite. However, x_{sur} values only slightly decrease with increasing preoxidation extent of magnetite and are all greater than those measured by wet chemistry (table S1), suggesting that the preoxidized magnetite forms an ordered Fe(II)-enriched outer layer. This result contradicts the prevailing view that the oxidation of magnetite leads to a core-shell magnetite-maghemite structure (*14*, *30*, *31*) and confirms observations made on similar magnetite particles (*12*, *17*, *34*). Spatially resolved STEM-HAADF with EELS was used to investigate the mechanism of magnetite oxidation and recharging and to confirm the formation of a Fe(II)-enriched surface layer (Fig. 2). The Fe L_3-edge EELS spectra

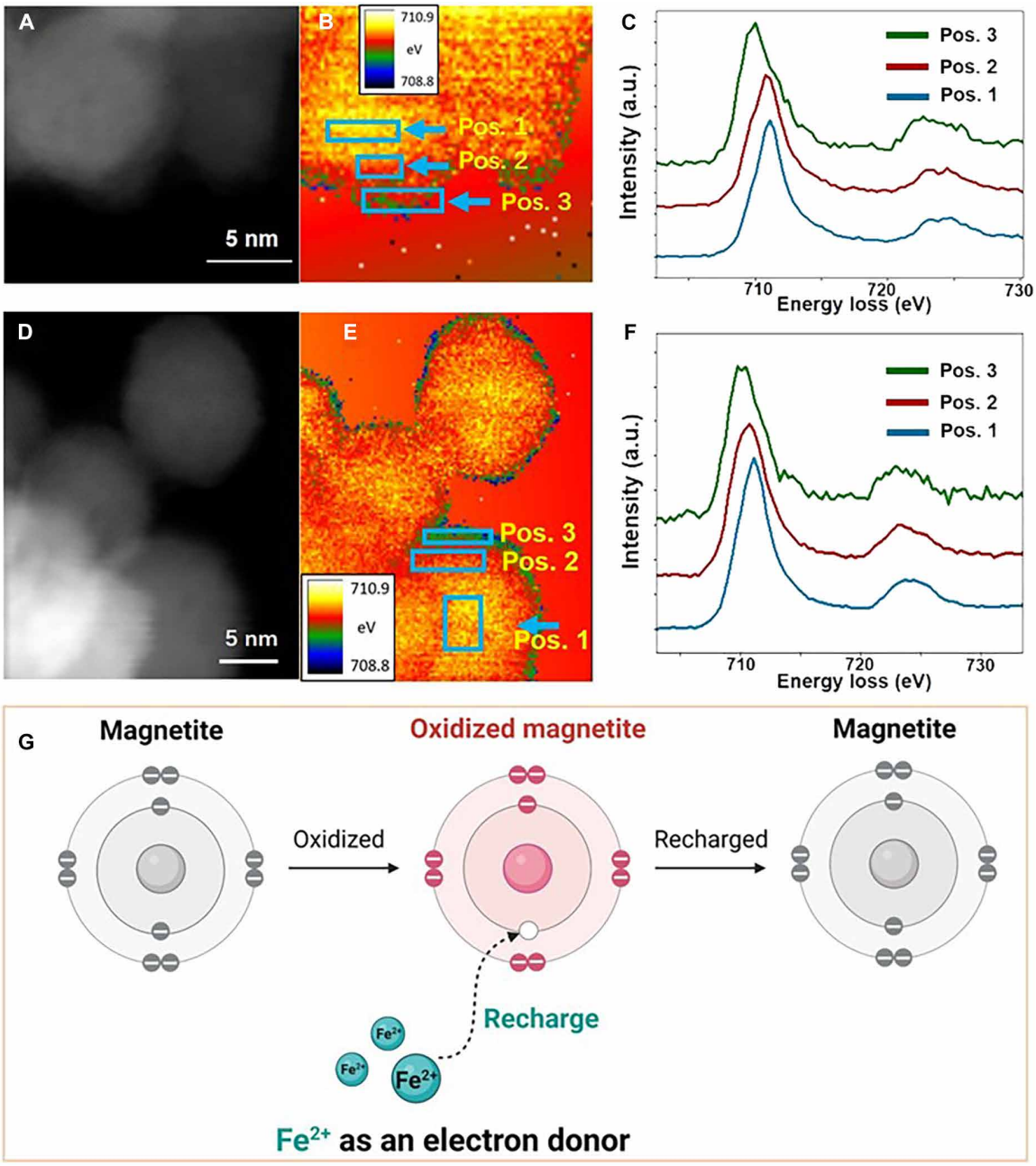

Fig. 2. Microscopic characterization and schematic illustration of preoxidized and recharged magnetite. Spim at the Fe L_3-edge of (**A** to **C**) $x = 0.2$ preoxidized magnetite, (**D** to **F**) $x = 0.2$ recharged magnetite, and (**G**) schematic illustration of magnetite oxidation and recharge. HAADF-STEM are in (A) and (D). The chemical shifts measured at the Fe L_3-edge are in (B) and (E). Spectra obtained at different positions (pos.) of the spim maps are shown in (C) and (F). a.u., arbitrary units.

show clear chemical shifts in Fig. 2 (B and E). From the Fe L_3-edge EELS spectra collected at different positions in the spectrum-imaging (spim) maps (Fig. 2, C and F), the peak position for the outermost layer (position 3) has the lowest energy, corresponding to a higher Fe(II) content. The layer beneath this (position 2) shows a mixture of Fe valence states, as in magnetite, and the peak position for the spectra collected in the core of the particle (position 1) has the highest energy, corresponding to a higher Fe(III) content. Thus, the spim maps confirm that both oxidized and recharged magnetite nanoparticles have a reduced shell, containing more Fe(II), and an oxidized core, containing more Fe(III). In addition, Mössbauer spectrometry measurements of x_{bulk} are basically consistent with those obtained via wet chemistry, both of which show lower values than those detected by XMCD. These results collectively confirm that the preoxidized magnetite forms a core-shell structure of maghemite-magnetite. Therefore, in contrast to the generally accepted magnetite oxidation mechanism, the internal Fe(II) diffuses to the surface forming a Fe(II)-enriched surface shell, with a highly oxidized core (Fig. 2G). When there is sufficient Fe(II) in solution for replenishment, the oxidized magnetite is recharged from the outside to regenerate magnetite. Moreover, the oxidation and recharging process only affects Fe atoms in the octahedral sites in the magnetite structure.

Re reduction with Fe^{2+}-recharged magnetite

After understanding the oxidation and recharging mechanisms of magnetite, Re was introduced into the system containing $Fe^{2+}_{(aq)}$ and (preoxidized) magnetite to investigate the fate of Re under these circumstances. Previous studies have shown that magnetite is more likely to dissolve at pH < 7.0 and to release Fe^{2+} due to proton-promoted dissolution, whereas Fe^{2+} uptake by magnetite is more favored at pH ≥ 8 (*35*). Thus, Re(VII) reduction experiments were performed at pH 6.5 and pH 8.0 with different amounts of Fe^{2+} addition to understand the effects of pH and different sources of Fe^{2+} (from dissolution or from external addition) on Re(VII) reduction (fig. S4). The results show that at pH 6.5, magnetite dissolves and Re(VII) is hardly adsorbed, regardless of whether Fe^{2+} is added to the suspension. In contrast, at pH 8.0, more Re is adsorbed at increasing Fe^{2+} concentration, and Re(VII) can be reductively sorbed only when Fe^{2+} is coadsorbed on magnetite. This suggests that pH plays a critical factor in the adsorption of Re(VII) on magnetite, presumably because pH influences the adsorption of Fe^{2+} on magnetite and, thus, the formation of a surface ternary complex and/or the reductive coprecipitation of Re(VII). Consequently, we selected pH 8.0 for further investigations, as this pH not only favors Re sorption on magnetite but is also environmentally relevant to several Fe-rich natural systems, such as marine Fe-rich sediments and Fe-rich subsurface environments (*40*–*42*). Less than 10% Re(VII) is adsorbed on preoxidized magnetite in the presence of 2.5 mM Fe^{2+} (fig. S5), as 2.5 mM Fe^{2+} is just enough to restore magnetite stoichiometry, i.e., 2.15 mM Fe^{2+} being required for $x = 0.33$ preoxidized magnetite to be recharged to $x = 0.5$. Moreover, when the supply of Fe^{2+} is less than that needed to restore the preoxidized magnetite, the coprecipitation of Re on magnetite is impeded, even at low Re(VII) concentrations (0.02 mM; fig. S6). These results confirm that an excess of $Fe^{2+}_{(aq)}$, beyond what is needed for recharging, is required for Re(VII) coprecipitation and reduction in preoxidized magnetite systems.

The added Fe^{2+} was then adjusted to 10 mM for all samples to compare the reduction of Re(VII) by preoxidized magnetite nanoparticles with a range of stoichiometries, in the presence of excess Fe^{2+}. Redox potential (Eh) and pH values were measured after 24-hour equilibration of (preoxidized) magnetite with 10 mM Fe^{2+} (fig. S7) and are reported in the Eh-pH diagram calculated for Fe using the Andra ThermoChimie database (Fig. 3A). The Eh-pH diagram indicates that there was plenty of Fe^{2+} in solution to react with maghemite for recharging under these experimental conditions. The results from Mössbauer spectrometry further substantiate that the $x = 0.20$ preoxidized magnetite has undergone complete recharge to the oxidation state of the starting material (fig. S8 and table S1). More oxidized (or less stoichiometric) magnetite takes up more Fe^{2+} (Fig. 3, B and C, and fig. S9), along with slower but almost complete adsorption of Re(VII) (Fig. 3, C and D). A higher initial concentration of Re leads to more Fe^{2+} adsorbed on magnetite (Fig. 3, B and C), which means that more Fe^{2+} is required for the reduction of the higher concentration of Re. The speciation of the resulting Re-solid species was explored using Re L_3-edge XANES spectroscopy (fig. S10). The Re L_3-edge XANES spectra show that 0.5 mM Re(VII) can be partially reduced by $x = 0.2$ preoxidized magnetite in the presence of external Fe^{2+} after 10 days, while very little or no reduction is observed at a Re(VII) concentration of 0.1 mM. On the other hand, Re(VII) can be almost completely reduced to Re(IV) by pure magnetite ($x = 0.5$) in the presence of 0.5 mM Fe^{2+} after a 30-day reaction, while Re(VII) is poorly adsorbed (only 1%) without additional Fe^{2+} and not reduced at all on pure magnetite, which is consistent with the literature reports that ReO_4^- is difficult to reduce by Fe oxides/hydroxides (*43*, *44*). These XANES results demonstrate that the addition of Fe^{2+} significantly promotes the adsorption and subsequent reduction of Re(VII) by pure/preoxidized magnetite, with the extent of reduction increasing with the initial Re concentration.

Recent studies of contaminant reduction by Fe^{2+}-amended Fe oxides reported a linear relationship between the logarithms of reduction rate constants and solid phase reduction potentials when electron transfer at the solid/solution interface occurs before or during the rate-limiting step of the reactions. The linear free energy relationship is also observed in this study. As shown in Fig. 3E, the rate constants (log k_{obs}; data shown in fig. S11 and table S2) for Re(VII) reduction were plotted versus the reduction potential (E_H) of (preoxidized) magnetite suspension equilibrated with Fe^{2+} at pH 8. The E_H value was estimated according to Eqs. 1 and 2

$$\gamma - Fe_2O_3 + 6H^+ + 2e^- = 2Fe^{2+} + 3H_2O \quad (1)$$

$$E_H = 185 - 177pH - 59\log\left[Fe^{2+}\right] \quad (2)$$

There is a linear correlation between log k_{obs} and pE (pE = E_H/0.059, the negative logarithm of the electron activity) for Fe^{2+} recharged magnetite at pH 8 (Fig. 3E), suggesting that the electron transfer process at the solid-solution interface is the rate-limiting step for Re(VII) reduction by Fe^{2+} recharged magnetite. On the other hand, Re(VII) reduction rates significantly increase with x value or Fe^{2+}_{ini} concentration. The faster Re(VII) reduction rates reflect the decrease of E_H for preoxidized magnetite/Fe^{2+} systems.

Insights into reaction mechanisms controlling Re speciation at the interface

Since $Fe^{2+}_{(aq)}$ cannot directly coprecipitate with Re(VII) to remove $Fe(ReO_4)_2$ from the solution (fig. S12), the reductive removal of Re(VII) requires first the adsorption of ReO_4^- onto the magnetite surface or rather its coadsorption as a ternary surface complex with

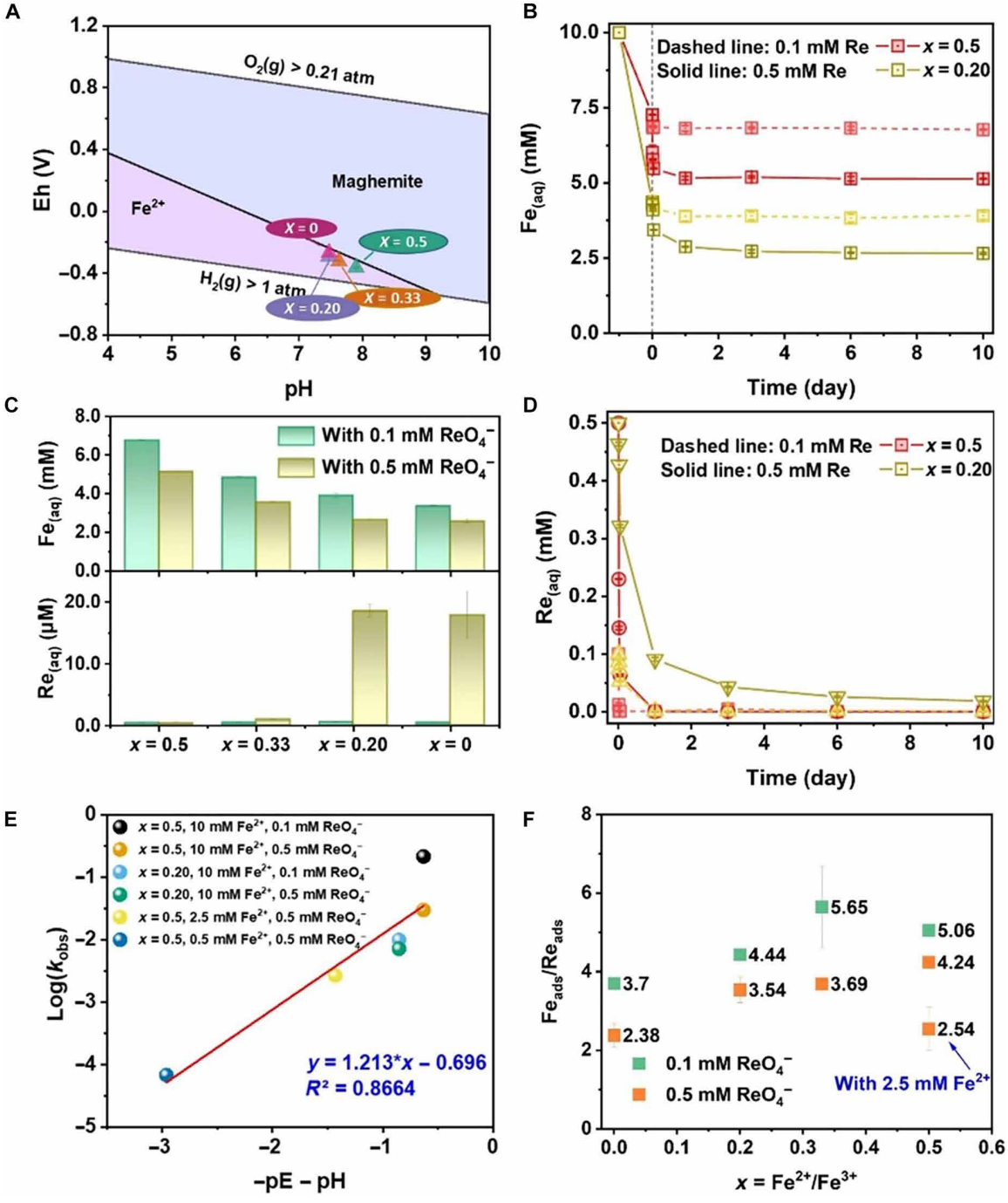

Fig. 3. Re reduction with Fe^{2+}-recharged magnetite. (**A**) Eh-pH diagram of Fe species (4 mM) in 0.1 M NaCl matrix and the measured Eh and pH after 24-hour equilibration of (preoxidized) magnetite with 10 mM Fe^{2+}, (**B** to **D**) $Fe_{(aq)}$ and $Re_{(aq)}$ concentrations in (preoxidized) magnetite suspension with the presence of 10 mM Fe^{2+} and 0.1 or 0.5 mM ReO_4^-, at pH 8.0, (**E**) the logarithms of the reduction rate constants [$\log(k_{obs})$] (in liters per minute) as a function of the calculated E_H values of $Fe^{2+}_{(aq)}$-amended magnetite, pE = E_H/0.059, and (**F**) Fe_{ads}/Re_{ads} as a function of the value of x with 10 mM Fe^{2+} (unless otherwise specified) at pH 8.0.

Fe^{2+}. At pH 8.0, the magnetite surface is negatively charged (pH_{pzc} = 6.5), and it is difficult for ReO_4^-, which also carries a single negative charge, to adsorb to the magnetite surface for reduction. However, the Fe^{2+} addition leads to a drop in the surface negative charge of pure/oxidized magnetite (fig. S13). This impact is slightly mitigated by the addition of Re(VII), possibly attributed to electrostatic attraction and the coprecipitation of ReO_4^- and Fe^{2+} on the magnetite surface. This finding is further supported by the promotion (at $t > 0$) of Fe^{2+} adsorption at pH 8.0 upon the addition of Re (fig. S4, A and B). The ratio of Fe adsorption to Re adsorption [Fe_{ads}/Re_{ads}; where Fe_{ads} equals Fe^{2+} concentration after 24-hour pre-equilibration minus the equilibrium concentration of Fe^{2+} after Re(VII) addition] was calculated (Fig. 3F) and reflects the redistribution of electrons between $Fe^{2+}_{(aq)}$, Re(VII), and magnetite.

Assuming that each system undergoes complete reduction of a Re(VII) to Re(IV), which requires three electrons from Fe^{2+}, an observed Fe_{ads}/Re_{ads} ratio around 5 in pure magnetite system indicates that part of Fe^{2+} is adsorbed by magnetite, potentially facilitating the overall electron transfer process, without contributing electrons. However, this ratio decreases as the oxidation extent of magnetite increases, implying that the adsorbed Fe^{2+} in the preoxidized magnetite system is also used for recharging the oxidized magnetite, in addition to Re(VII) reduction. The value of Fe_{ads}/Re_{ads} is slightly less than 3 with highly oxidized magnetite ($x = 0$), indicating that Re(VII) adsorbed has not been fully reduced.

Assuming that Re is fully sorbed on the magnetite surface, we calculated its maximum distribution density to assess whether sufficient adsorption sites were available to support Re reduction. The surface concentration of sorbed Re ranged from 0.43 to 2.15 atoms/nm^2 (fig. S14). Given that the site surface density of magnetite is 3.1 sites/nm^2 (*20*), this indicates that there are sufficient sites for Re sorption and that Re may be present as an incomplete monolayer on the surface. HAADF imaging is sensitive to the atomic number of elements (~$Z^{1.7}$), such that it is possible to discern individual Re atoms on top of the magnetite nanocrystals. On pure (i.e., fully recharged) magnetite particles, no distinct contrast is observed (Fig. 4A). However, individual surface Re atoms become discernible in the sample containing 0.1 mM Re (Fig. 4B, points at the arrow ends). In the case of $x = 0.2$ recharged magnetite with 0.5 mM Re, the Re atoms form small clusters, such as dimers, or longer ordered chains along the (111) crystallographic plane (Fig. 4C and fig. S15). Notably, the Re distribution is more pronounced in proximity to the edge of the particle (Fig. 4D), thereby confirming the sorption of Re at the surface of the magnetite. Re *M*-edge EELS was used to confirm that the difference in contrast in the HAADF images was due to the presence of Re, either for small clusters in the 0.5 mM Re sample (Fig. 3, D to G) or even for individual atoms in the case of the 0.1 mM Re sample (fig. S16).

Near the edge of the nanoparticles, Re dimers form clusters along the [−220] direction (fig. S15A, yellow circles). The position of the Re atoms often corresponds to a specific iron column (corresponding to the highest iron density—thus bright color—along that projection). An atomic model (fig. S15, B to E) shows two Re atoms (yellow), separated by a distance of ~0.30 nm, on top of these iron columns, as observed in the STEM images. The STEM imaging indicates that Re sits on top of (111) planes, as single atoms, dimers, or longer ordering, notably along the [220] direction. Fe L_3-edge EELS spectra reveal the presence of a surface layer that is enriched in Fe(II) with respect to the core of the particle, even after the reduction of Re(VII) at the surface of the recharged magnetite nanoparticles (Fig. 4, H to J). However, the surface layer was more enriched in Fe(II) for the recharged particles that had not been reacted with Re(VII) (Fig. 2, D to F). This is because reductive sorption of Re occurs on crystallographic edge sites, and this reductive adsorption can "block" further Fe^{2+} sorption and/or result in the immediate oxidation of Fe^{2+} with e^- being used to recharged magnetite. The Re L_3-edge EXAFS spectra (fig. S17) confirm the presence of second-neighbor metal shell at a $d_{Re\text{-}M}$ distance of 0.30 nm, with the metal being either Re in Re oxide surface polymers ($d_{Re\text{-}Re} = 0.31$ nm for edge-sharing octahedra) for the 0.5 mM Re samples or Fe when Re substitutes for structural Fe atoms at the surface (with $d_{Re\text{-}Fe} = 0.297$ nm for corner-sharing Fe octahedra) for the 0.1 mM Re samples, as suggested by STEM-EELS data. This is consistent with previous literature showing that elements such as Tc and As can substitute for Fe in the magnetite structure (*45*–*48*).

The combination of bulk and atomic scale techniques in this study provided sufficient information to propose a conceptual mechanistic model for Re(VII) reduction by recharged magnetite (Fig. 5): (i) Fe^{2+} in aqueous solution establishes ternary surface complexes with ReO_4^- at magnetite surface sites; (ii) Re(VII) is reduced along the crystallographic plane, such as (111), by Fe(II)-enriched magnetite, resulting in individual Re atoms or small clusters formed along (111) planes, with the core of the magnetite becoming oxidized; and (iii) the oxidized magnetite is recharged from the outside to regenerate magnetite with sufficient Fe^{2+} replenishment to achieve rapid Re(VII) reduction.

Implications of the magnetite recharge process on Re migration and transformation

The use of Re in paleoredox, geochronology, and environmental studies requires a more comprehensive understanding of its geochemistry. Solid-state cycling of $Fe^{2+}{}_{Oh}$ and $Fe^{3+}{}_{Oh}$ in magnetite is important for electron transfer between magnetite nanoparticles and Fe^{2+} in solution, and the recharging of magnetite by dissolved Fe^{2+} suggests that magnetite may be an important—and rechargeable—reductant for Re(VII) in ferruginous environments. Re(VII) behavior will therefore depend on the complex interactions between the chemical, hydrological, and physical conditions in the environment. The extent of Re enrichment in anoxic sediments underpins its use in the geological record and paleoenvironmental reconstruction (*49*). Therefore, understanding the interaction of Re(VII) with commonly occurring magnetite and $Fe^{2+}{}_{(aq)}$ ions under anoxic conditions will facilitate the interpretation of Re speciation data in geochronological, paleoredox, and environmental studies. In modern environments with elevated pollutant levels, the rapid removal of Re(VII) by Fe^{2+}-magnetite reactions is crucial for nuclear waste repository safety and the remediation of sites contaminated with radioactive Tc—an analog of Re that has been shown to form zigzag polymers of reduced Tc on magnetite surfaces (*24*, *50*).

Re resources are mainly contained in porphyry copper deposits, supplying ~80% of the Re mined (*51*). However, this study suggests that the presence of magnetite in aqueous phase rich in Fe^{2+} will lead to substantial Re deposition. The recharging mechanism is also assumed to occur between sediment bacteria and inorganic electron acceptors (*52*, *53*). This phenomenon is known as the "biogeobattery model" and can occur over long distances (at the meter scale). Along with the reduction of iron oxides by sediment bacteria, it may ultimately determine the fate of Fe and Re(VII) during redox cycling in the environment. Re-containing phases cannot normally be detected by x-ray diffraction due to their low content in the environment, but the presence of Re as a surficial phase on minerals in an ore body, as shown here in the STEM-EELS mapping for Re on magnetite, may be widely overlooked. More work is needed to address the potential role of these easily remobilized species in ore genesis and in situ recovery of Re from subsurface deposits.

We have shown that single Re atoms or small clusters form on the magnetite surface with the addition of Fe^{2+}. This discovery provides a simple and environmentally friendly method for the preparation of single-atom catalysts or cluster catalysts. Single-atom catalysts allow maximum atomic utilization and isolation of active sites and have become a prosperous branch of catalysis research in recent years. Re is often supported on CeO_2, SiO_2, and Al_2O_3 as a

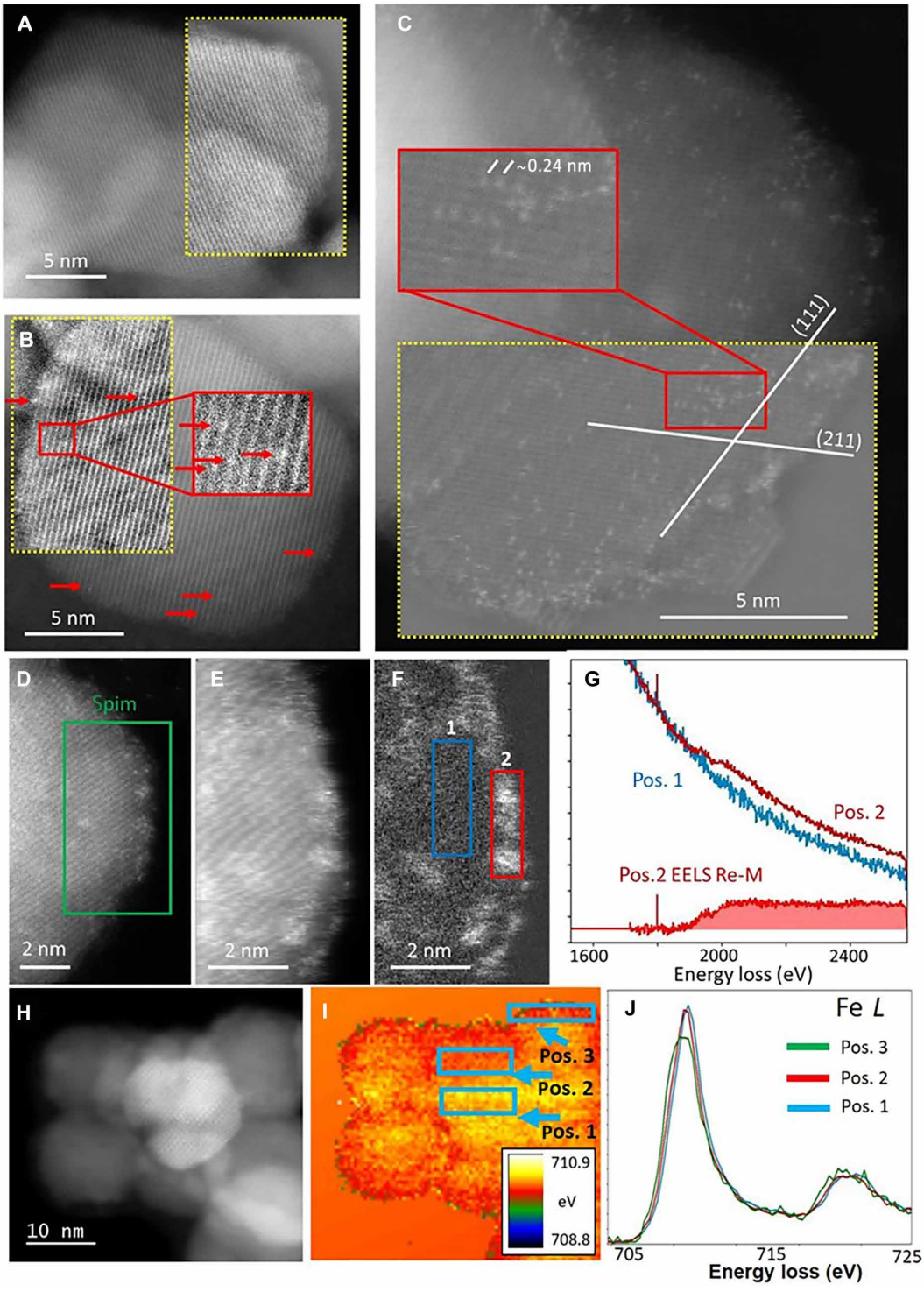

Fig. 4. Characterization by spatially resolved STEM-EELS. (**A** to **C**) HAADF STEM images of the (A) $x = 0.20$ recharged magnetite and $x = 0.20$ recharged magnetite in the presence of (B) 0.1 mM ReO_4^- and (C) 0.5 mM ReO_4^-. Some parts of the images are shown after background normalization to enhance the sharp contrast associated with individual or small clusters of Re atoms (yellow boxes). The HAADF-STEM images (**D**) before and (**E**) during the EELS spim acquisition, (**F**) chemical map from the Re *M*-edges, and (**G**) the EELS spectra extracted from a region with and without rhenium of $x = 0.20$ recharged magnetite in the presence of 0.5 mM ReO_4^-. (**H** to **J**) HAADF-STEM and spim at the Fe L_3-edges of $x = 0.20$ recharged magnetite in the presence of 0.1 mM ReO_4^-.

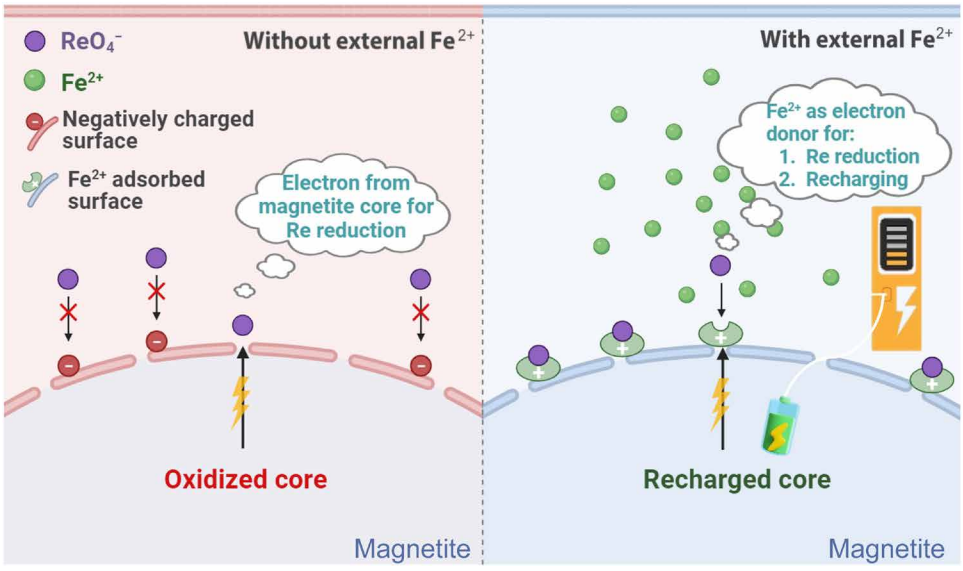

Fig. 5. Conceptual model of Re(VII) reduction by magnetite with the presence of $Fe^{2+}_{(aq)}$.

catalyst for water-splitting reactions or high value–added organic synthesis processes (*54*, *55*). Here, Fe^{2+} serves as an electron donor to supplement magnetite for the reductive precipitation of individual Re atoms (as well as other metal oxidants), while magnetite serves as a support for dispersing Re. The properties and applications of single–Re atom catalysts prepared by this method require further investigation.

MATERIALS AND METHODS

Materials

Magnetite was synthesized using the coprecipitation method in the N_2-filled glove box ($O_2 < 2$ parts per million). Specifically, a total of 240 ml of 6 M $NH_3{\cdot}H_2O$ solution was slowly added into a 200-ml mixture of 0.20 M Fe(II) solution ($FeCl_2{\cdot}4H_2O$) and 0.4 M Fe(III) solution ($FeCl_3{\cdot}6H_2O$) under stirring, and the resulting suspensions were aged for 1 day on a rotary shaker. Then, the solid particles were separated by a strong magnet and washed four times with degassed and deionized water (DDW) and two times with 0.1 mM NaCl solution, successively; the latter one was also used for its storage in an N_2-filled glove box.

Different sets of partially oxidized magnetite (25, 50, and 100%) were made by adding specific stoichiometric amounts of hydrogen peroxide (30% H_2O_2) to oxidize structural Fe(II) to Fe(III). The ratio of Fe(II)/Fe(III) (x) in all synthesized magnetite and preoxidized magnetite was determined by acid digestion, followed by spectrophotometric determination of dissolved Fe^{2+} using the 1,10-phenanthroline colorimetric method, and total Fe was measured by inductively coupled plasma optical emission spectrometry (ICP-OES).

Fe^{2+} uptake experiments

For Fe uptake experiments on partially oxidized magnetite, 2.15 to 8.62 mM $FeCl_2$ was added to preoxidized magnetite suspensions (2 g/liter) at pH 8.0 Hepes buffer [30 mM 4-(2-hydroxyethyl)-1-piperazineethanesulfonic acid], on the basis of the total amount of Fe^{2+} needed to bring the partially oxidized magnetite to $x = 0.5$. After 3 days of continuous shaking to allow Fe(II) release and enter the nanoparticles to reach equilibrium, 5 ml of suspension samples were filtered through a syringe filter (0.22 μm) and used for ICP-OES analyses. Solids were collected by vacuum filtration for further characterization.

ReO_4^- reduction experiments

ReO_4^- reduction experiments were conducted at pH 6.5 MES buffer [30 mM 2-(*N*-morpholino)ethanesulfonic acid] and pH 8.0 Hepes buffer. Reduction experiments were initiated by adding 0 to 0.5 mM ReO_4^- to the suspension of (preoxidized) magnetite (2 g/liter) after the 24-hour equilibration period with a certain concentration of Fe^{2+} (0 to 10 mM). At selected time intervals, 5-ml suspension was sampled and filtered through a syringe filter (0.22 μm) and used for ICP-OES analyses. Solid was collected by vacuum filtration for further analysis.

Analytical methods

The pH of the suspension was measured using a combined glass micro-pH electrode (Metrohm 6.0234.100) after calibrating with pH 4.00, 7.01, 10.00, and 12.00 standard solutions. Eh was measured through a combined Pt-ring ORP electrode (Metrohm 6.0451.100), calibrated with Zobell's solution (200 mV at 25°C). Concentrations of Re and Fe were analyzed using ICP-OES with a Varian 720-ES instrument. Zeta potential was measured using a Zetasizer Nano ZS instrument (Malvern Instruments, Malvern, UK).

^{57}Fe Mössbauer spectroscopy was used to determine the stoichiometry of magnetite before and after the reaction. The measurements were conducted at 77 and 300 K using a transmission geometry setup, with a 925 MBq of γ-source of ^{57}Co/Rh mounted on a conventional constant acceleration drive. The samples, containing Fe (~5 mg/cm^2), were prepared and sealed with epoxy glue in a glove box. Subsequently, they were transferred under N_2-filled conditions. The hyperfine structures were analyzed using the custom MOSFIT program (*56*), which uses Lorentzian lines to fit magnetic sextets.

RIXS, XANES, and EXAFS data were collected at the Rossendorf Beamline (BM20) of the European Synchrotron Radiation Facility (ESRF). RIXS spectroscopy was used to characterize the distribution of total Fe in the bulk materials, including both ordered and disordered Fe, with measurements conducted at the Fe *K*-edge. We measured commercial magnetite and hematite as standards for comparison, ensuring the accuracy and reliability of our results. After data collection, the RIXS data were analyzed using PyXES software, which allowed us to obtain an enlargement of the pre-edge features in the *K*-edge spectra. This analysis involved extracting related partial fluorescence-yield XANES from RIXS planes using the signal at the maximum of the emission spectra, along with diagonal cuts across the RIXS plane at CEE for detailed examination (*57*). EXAFS and XANES were used to investigate the chemical environment and oxidation states of Re, performed at the Re L_3-edge. $NaReO_4$ and ReO_2 were analyzed as standards for reference. The x-ray beam energy was tuned using a Si(111) crystal pair in pseudo–channel cut mode, controlled by a doubled crystal monochromator. Fluorescence spectra were recorded using a high-purity germanium detector (Ultra-LEGe, GUL0055, Mirion Technologies). For EXAFS and XANES data analysis, we used the Athena software from the Demeter package (*58*). All samples were double-face sealed using polyimide tape in an N_2-filled glove box. They were then mounted on a sample holder and stored in an N_2-filled aluminum envelope before being transferred to the vacuum experimental chamber. To mitigate the effects of thermal disorder caused by atomic vibrations, the temperature was lowered to 77 K using a liquid N_2 cryostat.

Samples used for XMCD measurements were prepared in the N_2-filled glove box. Magnetite was dried and loaded onto carbon tape affixed to a sample holder. The sample manipulator was loaded into the end station under anaerobic conditions. The sample was positioned with the x-ray beam entering parallel to the magnetic field and perpendicular to the sample surface. X-ray absorption spectra at the Fe $L_{2,3}$-edges were collected at room temperature on beamline 4.0.2 at the Advanced Light Source in Berkeley, CA using an eight-pole resistive magnet end-station (*59*). Beamline 4.0.2 is equipped with an elliptically polarizing undulator source and a variable-included angle monochromator, providing soft x-rays with a resolving power near 6000 at the Fe $L_{2,3}$-edges (*60*).The x-ray absorption spectrum (XAS) was monitored in total electron yield mode. At each energy point, the XAS were measured for two opposite magnetization directions by reversing the applied field of 0.4 T. After normalization to the incident beam intensity, the XMCD spectrum was obtained as the difference between the two XAS (*61*). Following the collection of XMCD data, a nonlinear least-squares analysis of the XMCD spectra was conducted to quantify the surface-localized Fe^{2+}/Fe^{3+} ratios (x_{sur}) of magnetite (*36*, *62*). To obtain the relative amounts of Fe on the three sites, the experimental spectra were fitted by means of a nonlinear least-squares analysis, using calculated spectra for each of the Fe sites (*63*). The effective probing depth of XMCD is ~4 to 5 nm (*33*, *64*), while the particle size of the magnetite is around 15 to 20 nm. However, given the exponential signal decay into the nanoparticles, it is reasonable to assume that the XMCD spectra report primarily just on the upper few angstroms of the nanoparticle surfaces (*65*).

Samples used for STEM-HAADF and EELS measurements were prepared in the anaerobic chamber using diluted suspensions in DDW. They were then dropped cast onto holey amorphous carbon Cu grids (Agar Scientific Ltd.), left to dry in the anaerobic chamber, and further dehydrated with a drop of ethanol. Samples were transferred to the Cs aberration–corrected STEM in a grid box wrapped in parafilm, loaded into a double tilt FEI TEM holder, and inserted into the STEM; the grid was exposed to air for approximately less than 60 s. The NION UltraSTEM200 operated at 100 kV and was coupled with a high-sensitivity EEL spectrometer. The spectrum image was obtained by analyzing the transmitted electron beam at each probed position with the spectrometer. The total dataset was typically formed by ~100 pixels by 100 pixels (spectra) with a beam spot size of 0.1 nm, pixel sizes from 30 to 100 pm, and the acquisition time of each spectrum from 2 to 10 ms. In all cases, data were collected from clean GR plates, those that were considered free of contamination and/or visible stray iron (oxyhydr)oxide minerals of different valence ratios.

Supplementary Materials

This PDF file includes:

Figs. S1 to S17
Tables S1 and S2

REFERENCES AND NOTES

1. A. D. Anbar, R. A. Creaser, D. A. Papanastassiou, G. J. Wasserburg, Rhenium in seawater: Confirmation of generally conservative behavior. *Geochim. Cosmochim. Acta* **56**, 4099–4103 (1992).
2. A. Poirier, C. Hillaire-Marcel, Improved Os-isotope stratigraphy of the Arctic Ocean. *Geophys. Res. Lett.* **38**, L14607 (2011).
3. C. A. Miller, B. Peucker-Ehrenbrink, E. A. Schauble, Theoretical modeling of rhenium isotope fractionation, natural variations across a black shale weathering profile, and potential as a paleoredox proxy. *Earth Planet. Sci. Lett.* **430**, 339–348 (2015).
4. D. A. John, R. D. Taylor, P. L. Verplanck, M. W. Hitzman, in *Rare Earth and Critical Elements in Ore Deposits* (Society of Economic Geologists, 2016), vol. 18, pp. 137–164.
5. W. W. Bennett, D. E. Canfield, Redox-sensitive trace metals as paleoredox proxies: A review and analysis of data from modern sediments. *Earth Sci. Rev.* **204**, 103175 (2020).
6. B. Kendall, R. A. Creaser, C. T. Reinhard, T. W. Lyons, A. D. Anbar, Transient episodes of mild environmental oxygenation and oxidative continental weathering during the late Archean. *Sci. Adv.* **1**, e1500777 (2015).
7. A. Chappaz, C. Gobeil, A. Tessier, Sequestration mechanisms and anthropogenic inputs of rhenium in sediments from Eastern Canada lakes. *Geochim. Cosmochim. Acta* **72**, 6027–6036 (2008).
8. D. G. Brookins, Rhenium as analog for fissiogenic technetium: Eh-pH diagram (25°C, 1 bar) constraints. *Appl. Geochem.* **1**, 513–517 (1986).
9. C. A. Miller, B. Peucker-Ehrenbrink, B. D. Walker, F. Marcantonio, Re-assessing the surface cycling of molybdenum and rhenium. *Geochim. Cosmochim. Acta* **75**, 7146–7179 (2011).
10. R. Liao, C. Li, H. Liu, Q. Chen, W. Sun, Rhenium enrichment in the northwest Pacific arc. *Ore Geol. Rev.* **115**, 103176 (2019).
11. Y. Li, Comparative geochemistry of rhenium in oxidized arc magmas and MORB and rhenium partitioning during magmatic differentiation. *Chem. Geol.* **386**, 101–114 (2014).
12. B. A. Calhoun, Magnetic and electric properties of magnetite at low temperatures. *Phys. Rev.* **94**, 1577–1585 (1954).
13. B. Maher, Ubiquitous magnetite. *Nat. Geosci.* **17**, 7 (2024).
14. I. A. M. Ahmed, B. A. Maher, Identification and paleoclimatic significance of magnetite nanoparticles in soils. *Proc. Natl. Acad. Sci. U.S.A.* **115**, 1736–1741 (2018).
15. H. Wang, D. V. Kent, M. J. Jackson, Evidence for abundant isolated magnetic nanoparticles at the Paleocene–Eocene boundary. *Proc. Natl. Acad. Sci. U.S.A.* **110**, 425–430 (2013).
16. X. Yan, Q. Zhou, M. Vincent, Y. Deng, J. Yu, J. Xu, T. Xu, T. Tang, L. Bian, Y.-X. J. Wang, K. Kostarelos, L. Zhang, Multifunctional biohybrid magnetite microrobots for imaging-guided therapy. *Sci. Robot.* **2**, eaaq1155 (2017).
17. J. M. Byrne, N. Klueglein, C. Pearce, K. M. Rosso, E. Appel, A. Kappler, Redox cycling of Fe(II) and Fe(III) in magnetite by Fe-metabolizing bacteria. *Science* **347**, 1473–1476 (2015).
18. C. A. Gorski, R. M. Handler, B. L. Beard, T. Pasakarnis, C. M. Johnson, M. M. Scherer, Fe atom exchange between aqueous Fe^{2+} and magnetite. *Environ. Sci. Technol.* **46**, 12399–12407 (2012).
19. R. Bliem, E. McDermott, P. Ferstl, M. Setvin, O. Gamba, J. Pavelec, M. A. Schneider, M. Schmid, U. Diebold, P. Blaha, L. Hammer, G. S. Parkinson, Subsurface cation vacancy stabilization of the magnetite (001) surface. *Science* **346**, 1215–1218 (2014).
20. C. A. Gorski, M. M. Scherer, Influence of magnetite stoichiometry on Fe^{II} uptake and nitrobenzene reduction. *Environ. Sci. Technol.* **43**, 3675–3680 (2009).
21. C. A. Gorski, M. S. Fantle, Stable mineral recrystallization in low temperature aqueous systems: A critical review. *Geochim. Cosmochim. Acta* **198**, 439–465 (2017).

22. A. C. Scheinost, L. Charlet, Selenite reduction by mackinawite, magnetite and siderite: XAS characterization of nanosized redox products. *Environ. Sci. Technol.* **42**, 1984–1989 (2008).
23. A. Poulain, A. Fernandez-Martinez, J. M. Greneche, D. Prieur, A. C. Scheinost, N. Menguy, S. Bureau, V. Magnin, N. Findling, J. Drnec, I. Martens, M. Mirolo, L. Charlet, Selenium nanowire formation by reacting selenate with magnetite. *Environ. Sci. Technol.* **56**, 14817–14827 (2022).
24. E. Bianchetti, A. F. Oliveira, A. C. Scheinost, C. Di Valentin, G. Seifert, Chemistry of the interaction and retention of Tc^{VII} and Tc^{IV} species at the $Fe_3O_4(001)$ surface. *J. Phys. Chem. C* **127**, 7674–7682 (2023).
25. K. Yuan, E. S. Ilton, M. R. Antonio, Z. R. Li, P. J. Cook, U. Becker, Electrochemical and spectroscopic evidence on the one-electron reduction of U(VI) to U(V) on magnetite. *Environ. Sci. Technol.* **49**, 6206–6213 (2015).
26. Z. Z. Pan, B. Bártová, T. LaGrange, S. M. Butorin, N. C. Hyatt, M. C. Stennett, K. O. Kvashnina, R. Bernier-Latmani, Nanoscale mechanism of UO_2 formation through uranium reduction by magnetite. *Nat. Commun.* **11**, 4001 (2020).
27. D. E. Latta, B. Mishra, R. E. Cook, K. M. Kemner, M. I. Boyanov, Stable U(IV) complexes form at high-affinity mineral surface sites. *Environ. Sci. Technol.* **48**, 1683–1691 (2014).
28. K. Wang, A. F. Martinez, L. Simonelli, B. Madé, P. Hénocq, B. Ma, L. Charlet, Redox interaction between selenite and mackinawite in cement pore water. *Environ. Sci. Technol.* **56**, 5602–5610 (2022).
29. J. R. Bargar, K. H. Williams, K. M. Campbell, P. E. Long, J. E. Stubbs, E. I. Suvorova, J. S. Lezama-Pacheco, D. S. Alessi, M. Stylo, S. M. Webb, J. A. Davis, D. E. Giammar, L. Y. Blue, R. Bernier-Latmani, Uranium redox transition pathways in acetate-amended sediments. *Proc. Natl. Acad. Sci. U.S.A.* **110**, 4506–4511 (2013).
30. J. Tang, M. Myers, K. A. Bosnick, L. E. Brus, Magnetite Fe_3O_4 nanocrystals: Spectroscopic observation of aqueous oxidation kinetics. *J. Phys. Chem. B* **107**, 7501–7506 (2003).
31. S. J. Iyengar, M. Joy, C. K. Ghosh, S. Dey, R. K. Kotnala, S. Ghosh, Magnetic, x-ray and Mössbauer studies on magnetite/maghemite core–shell nanostructures fabricated through an aqueous route. *RSC Adv.* **4**, 64919–64929 (2014).
32. T. Kim, S. Sim, S. Lim, M. A. Patino, J. Hong, J. Lee, T. Hyeon, Y. Shimakawa, S. Lee, J. P. Attfield, J.-G. Park, Slow oxidation of magnetite nanoparticles elucidates the limits of the Verwey transition. *Nat. Commun.* **12**, 6356 (2021).
33. J. M. Byrne, G. van der Laan, A. I. Figueroa, O. Qafoku, C. Wang, C. I. Pearce, M. Jackson, J. Feinberg, K. M. Rosso, A. Kappler, Size dependent microbial oxidation and reduction of magnetite nano- and micro-particles. *Sci. Rep.* **6**, 30969 (2016).
34. H. Peng, C. I. Pearce, A. T. N'Diaye, Z. Zhu, J. Ni, K. M. Rosso, J. Liu, Redistribution of electron equivalents between magnetite and aqueous Fe^{2+} induced by a model quinone compound AQDS. *Environ. Sci. Technol.* **53**, 1863–1873 (2019).
35. H. Peng, C. I. Pearce, W. F. Huang, Z. Zhu, A. T. N'Diaye, K. M. Rosso, J. Liu, Reversible Fe(II) uptake/release by magnetite nanoparticles. *Environ. Sci. Nano* **5**, 1545–1555 (2018).
36. J. Liu, C. I. Pearce, O. Qafoku, E. Arenholz, S. M. Heald, K. M. Rosso, Tc(VII) reduction kinetics by titanomagnetite ($Fe_{3-x}Ti_xO_4$) nanoparticles. *Geochim. Cosmochim. Acta* **92**, 67–81 (2012).
37. K. J. Gallagher, W. Feitknecht, U. Mannweiler, Mechanism of oxidation of magnetite to γ-Fe_2O_3. *Nature* **217**, 1118–1121 (1968).
38. K. Yuan, S. S. Lee, W. Cha, A. Ulvestad, H. Kim, B. Abdilla, N. C. Sturchio, P. Fenter, Oxidation induced strain and defects in magnetite crystals. *Nat. Commun.* **10**, 703 (2019).
39. M. L. Baker, M. W. Mara, J. J. Yan, K. O. Hodgson, B. Hedman, E. I. Solomon, K- and L-edge x-ray absorption spectroscopy (XAS) and resonant inelastic x-ray scattering (RIXS) determination of differential orbital covalency (DOC) of transition metal sites. *Coord. Chem. Rev.* **345**, 182–208 (2017).
40. L. Heinrich, M. Rothe, B. Braun, M. Hupfer, Transformation of redox-sensitive to redox-stable iron-bound phosphorus in anoxic lake sediments under laboratory conditions. *Water Res.* **189**, 116609 (2021).
41. C. Spiteri, P. Regnier, C. P. Slomp, M. A. Charette, pH-dependent iron oxide precipitation in a subterranean estuary. *J. Geochem. Explor.* **88**, 399–403 (2006).
42. C. Tanvet, E. F. Camp, J. Sutton, F. Houlbrèque, G. Thouzeau, R. Rodolfo-Metalpa, Corals adapted to extreme and fluctuating seawater pH increase calcification rates and have unique symbiont communities. *Ecol. Evol.* **13**, e10099 (2023).
43. B. E. Anderson, U. Becker, K. B. Helean, R. C. Ewing, Perrhenate and pertechnetate behavior on iron and sulfur-bearing compounds. *MRS Online Proc. Library* **985**, 1209 (2006).
44. M. J. Wharton, B. Atkins, J. M. Charnock, F. R. Livens, R. A. D. Pattrick, D. Collison, An x-ray absorption spectroscopy study of the coprecipitation of Tc and Re with mackinawite (FeS). *Appl. Geochem.* **15**, 347–354 (2000).
45. E. Yalçıntaş, A. C. Scheinost, X. Gaona, M. Altmaier, Systematic XAS study on the reduction and uptake of Tc by magnetite and mackinawite. *Dalton Trans.* **45**, 17874–17885 (2016).
46. B. L. Huhmann, A. Neumann, M. I. Boyanov, K. M. Kemner, M. M. Scherer, Emerging investigator series: As(V) in magnetite: Incorporation and redistribution. *Environ. Sci.: Processes Impacts* **19**, 1208–1219 (2017).
47. J. P. H. Perez, D. J. Tobler, H. M. Freeman, A. P. Brown, N. S. Hondow, C. M. van Genuchten, L. G. Benning, Arsenic species delay structural ordering during green rust sulfate crystallization from ferrihydrite. *Environ. Sci. Nano* **8**, 2950–2963 (2021).
48. C. M. van Genuchten, The enhanced stability of arsenic coprecipitated with magnetite during aging: An XAS investigation. *Ind. Eng. Chem. Res.* **61**, 13154–13167 (2022).
49. D. R. Hummer, J. J. Golden, G. Hystad, R. T. Downs, A. Eleish, C. Liu, J. Ralph, S. M. Morrison, M. B. Meyer, R. M. Hazen, Evidence for the oxidation of Earth's crust from the evolution of manganese minerals. *Nat. Commun.* **13**, 960 (2022).
50. A. F. Oliveira, A. Kuc, T. Heine, U. Abram, A. C. Scheinost, Shedding light on the enigmatic $TcO_2 \cdot xH_2O$ structure with density functional theory and EXAFS spectroscopy. *Chem. A Eur. J.* **28**, e202202235 (2022).
51. A. I. Grabezhev, Rhenium in porphyry copper deposits of the urals. *Ore Geol. Rev.* **55**, 13–26 (2013).
52. L. P. Nielsen, N. Risgaard-Petersen, H. Fossing, P. B. Christensen, M. Sayama, Electric currents couple spatially separated biogeochemical processes in marine sediment. *Nature* **463**, 1071–1074 (2010).
53. A. Revil, C. A. Mendonça, E. A. Atekwana, B. Kulessa, S. S. Hubbard, K. J. Bohlen, Understanding biogeobatteries: Where geophysics meets microbiology. *J. Geophys. Res. Biogeosci.* **115**, G00G02 (2010).
54. K. S. Vargas, J. Zaffran, M. Araque, M. Sadakane, B. Katryniok, Deoxydehydration of glycerol to allyl alcohol catalysed by ceria-supported rhenium oxide. *Mol. Catal.* **535**, 112856 (2023).
55. A. M. R. Ramírez, S. Heidari, A. Vergara, M. V. Aguilera, P. Preuss, M. B. Camarada, A. Fischer, Rhenium-based electrocatalysts for water splitting. *ACS Mater. Au* **3**, 177–200 (2023).
56. R. J. Joseyphus, J. M. Greneche, in *Fundamentals of ^{57}Fe Mössbauer Spectrometry*, R. J. Joseyphus, J.-M. Greneche, Eds. (Springer, 2024), pp. 265–299.
57. K. O. Kvashnina, A. C. Scheinost, A Johann-type x-ray emission spectrometer at the Rossendorf beamline. *J. Synchrotron Radiat.* **23**, 836–841 (2016).
58. B. Ravel, M. Newville, *ATHENA*, *ARTEMIS*, *HEPHAESTUS*: Data analysis for x-ray absorption spectroscopy using *IFEFFIT*. *J. Synchrotron Radiat.* **12**, 537–541 (2005).
59. E. Arenholz, S. O. Prestemon, Design and performance of an eight-pole resistive magnet for soft x-ray magnetic dichroism measurements. *Rev. Sci. Instrum.* **76**, 083908 (2005).
60. A. T. Young, J. Feng, E. Arenholz, H. A. Padmore, T. Henderson, S. Marks, E. Hoyer, R. Schlueter, J. B. Kortright, V. Martynov, C. Steier, G. Portmann, First commissioning results for the elliptically polarizing undulator beamline at the Advanced Light Source. *Nucl. Instrum. Methods Phys. Res. Sec. A* **467-468**, 549–552 (2001).
61. R. A. D. Pattrick, G. Van Der Laan, C. M. B. Henderson, P. Kuiper, E. Dudzik, D. J. Vaughan, Cation site occupancy in spinel ferrites studied by x-ray magnetic circular dichroism: Developing a method for mineralogists. *Eur. J. Mineral.* **14**, 1095–1102 (2002).
62. G. Van der Laan, I. W. Kirkman, The 2p absorption spectra of 3d transition metal compounds in tetrahedral and octahedral symmetry. *J. Phys. Condens. Matter* **4**, 4189–4204 (1992).
63. C. I. Pearce, C. M. B. Henderson, N. D. Telling, R. A. D. Pattrick, J. M. Charnock, V. S. Coker, E. Arenholz, F. Tuna, G. van der Laan, Fe site occupancy in magnetite-ulvospinel solid solutions: A new approach using x-ray magnetic circular dichroism. *Am. Mineral.* **95**, 425–439 (2010).
64. S. Gota, M. Gautier-Soyer, M. Sacchi, Fe *2p* absorption in magnetic oxides: Quantifying angular-dependent saturation effects. *Phys. Rev. B* **62**, 4187–4190 (2000).
65. J. Liu, C. I. Pearce, C. Liu, Z. Wang, L. Shi, E. Arenholz, K. M. Rosso, $Fe_{3-x}Ti_xO_4$ nanoparticles as tunable probes of microbial metal oxidation. *J. Am. Chem. Soc.* **135**, 8896–8907 (2013).

Acknowledgments: This work was a collaboration between the Charlet group and Rosso group. Synchrotron experiments were performed on beamline BM20 at the ESRF, Grenoble, France under user proposal EV-522 and on beamline 6.3.1 at the Advanced Light Source (ALS), Berkeley, CA using the eight-pole resistive magnet end-station. **Funding:** C.G. acknowledges funding support from Convocatoria 885 (2021–2024), Ministry of Science, Technology, and Innovation, Colombia. R.D. and L.C. acknowledge support from MITI-CNRS grant no. 268450 and the Chinese Scholarship Council. K.M.R., C.I.P., and E.A. acknowledge support from the US Department of Energy, Office of Science, Office of Basic Energy Sciences, Chemical Sciences, Geosciences, and Biosciences Division through its Geosciences program at Pacific Northwest National Laboratory (FWP 56674). R.D. and Y.M. also acknowledge the support from the National Natural Science Foundation of China (52025101). **Author contributions:** Conceptualization: R.D., K.M.R., and L.C. Methodology: All authors. Investigation: R.D., C.I.P., E.A., J.-M.G., and A.G. Supervision: Y. M. and L.C. Writing—original draft: R.D., Y.M., K.M.R., and L.C. Writing—review and editing: All authors. **Competing interests:** The authors declare that they have no competing interests. **Data and materials availability:** All data needed to evaluate the conclusions in the paper are present in the paper and/or the Supplementary Materials.

Submitted 16 May 2024
Accepted 14 April 2025
Published 16 May 2025
10.1126/sciadv.adq3650